AIChE

Master Curves for Mass Transfer in Bidisperse Adsorbents for Pressure-Swing and Volume-Swing Frequency Response Methods

Yu Wang and M. Douglas LeVan
Dept. of Chemical and Biomolecular Engineering, Vanderbilt University, Nashville, TN 37235

DOI 10.1002/aic.12420
Published online October 12, 2010 in Wiley Online Library (wileyonlinelibrary.com).

A general model has been developed for pressure-swing and volume-swing frequency response methods with analytical solutions derived to analyze various mass transfer resistances in biporous adsorbents. The model can consider a combination of distributed mass transfer resistances acting independently or in series including macropore diffusion, micropore diffusion, and a surface barrier resistance at the entrance of micropores. Heat effects are included for nonisothermal systems. Temperature variations are shown to be less for pressure-swing compared with volume-swing systems. The general model is developed in such a way that information extracted from it is independent of whether a system is batch volume swing or flow-through pressure swing. Simulation results demonstrate that mass transfer mechanisms can be easily discriminated by the master curves. Isothermal models exhibit one-step curves, whereas nonisothermal effects are represented by two-step curves. Examples are given to demonstrate the use of the master curves to describe experimental data. © 2010 American Institute of Chemical Engineers *AIChE J,* 57: 2054–2069, 2011
Keywords: adsorption/gas, diffusion (microporous), mass transfer, frequency response, biporous material

Introduction

Knowledge of mass transfer rates is important for understanding transport phenomena inside porous adsorbents and catalysts as well as for the design of adsorption and catalytic processes. Mass transfer in materials can be a complex phenomenon as it is strongly influenced by the structure of the solid, the system, and the precise process conditions. One or more mass transfer steps can be rate controlling, such as pore diffusion, micropore diffusion (surface diffusion), or a surface barrier resistance. Because of the complicated mass transfer characteristics that can be encountered, the frequency response (FR) method has been shown to be promising because of its ability to discriminate easily among different rate-limiting mechanisms.[1]

The most common method used for estimating a mass transfer resistance is a simple step test. The concentration in a system is increased in a step and the response of particles is measured gravimetrically, volumetrically, or chromatographically. A particular mass transfer model is assumed, and the system response is fitted to obtain a rate parameter. This approach generally fails to identify in any rigorous way the controlling mass transfer resistance. Heat effects are often ignored, system nonlinearities caused by large steps are not identified, and fit parameters typically are often of little general significance.

When compared with common step methods, FR is a perturbation technique that is carried out around equilibrium. Thus, it has less experimental error as the results are obtained from periodic measurements and are not dependent

Correspondence concerning this article should be addressed to M. D. LeVan at m.douglas.levan@vanderbilt.edu.

on the initial, preperiodic state. Moreover, the frequency of oscillations introduces an additional degree of freedom that can be used to decouple individual steps occurring with different characteristic relaxation times.

Most theoretical and experimental aspects of FR have been studied for a batch system in which gas pressure is changed by a forced periodic volume fluctuation.[1–9] Yasuda applied this volume-swing technique with an isothermal model to study physical and chemical phenomena occurring on zeolites, including adsorption,[2,10] diffusion–controlled processes,[11–13] combinations of adsorption–diffusion processes,[14] and reactions.[15–18] Rees and coworkers[8,9,19] used a square-wave volume perturbation instead of the traditional sinusoidal wave to investigate hydrocarbons adsorbed on silicate adsorbents. Jordi and Do[6,7] have developed thorough theoretical models for both isothermal and nonisothermal conditions to study volume perturbation in a batch system and derived analytical solutions for the characteristic functions for biporous materials. Sun and coworkers[1,20–23] investigated heat effects theoretically and experimentally with a volume frequency response method or a thermal frequency response method. They found that the intrusion of heat effects can also lead to a bimodal FR if the rate of heat transfer is sufficiently slower than the mass diffusion. Bimodal behavior has also been observed in biporous materials and explained well by an isothermal macropore and micropore diffusion model or two independent diffusion models.

In addition to the studies on batch systems, there have been other applications in flow systems involving concentration variations.[24–29] We have developed the flow-through pressure-swing (PSFR) and concentration-swing frequency response (CSFR) methods to study mass transfer rates for both pure and mixed gases and vapors and have applied the methods to carbon molecular sieve (CMS), silica gel, and activated carbon materials.[30–35] Mass transfer of pure N_2 and CH_4 is mainly controlled by the surface barrier resistance at the pore mouth of the CMS, whereas that for O_2 is controlled by both micropore diffusion and a barrier resistance, and for CO_2 is controlled solely by micropore diffusion.[32,35] Mixtures of these components have been studied by both PSFR and CSFR, and the main-term and cross-term diffusivities have been obtained for different concentrations with mixture models.[32,34] Mass–transfer rates of pure chloroethane on activated carbon have been studied by both systems and the results are in good agreement. Furthermore, heat effects have been shown to be often negligible for CSFR but often apparent for PSFR because of operating conditions. Axial dispersion has been considered and can be easily recognized by the CSFR method.[31]

The classical linear FR method has been extended by Petkovska et al.[36–39] to the nonlinear case by applying the mathematical tools of the Volterra series and the concept of higher order frequency response functions. With the analysis of the second-order frequency response functions, the nonlinear FR method enables discrimination of mass-transfer mechanisms that have bimodal characteristic functions and can be fitted well by several models from the linear volume perturbation FR.[37]

In this research, we develop a general model to describe distributed mass transfer resistances in bidisperse materials for both the PSFR flow-through and VSFR batch systems. This work expands upon and completes a previous model of ours[35] with consideration of resistances in both macropore and micropore regions with or without a surface barrier resistance. Additionally, theoretical studies are carried out for comparison of distributed mass transfer resistances. Each model can be represented by a distinctive master curve, which is a function of the ratio of perturbation frequency to system intrinsic mass-transfer rate. With this approach, the characteristic curves are general, with a single curve describing all mass transfer rates for a given mechanism for both PSFR and VSFR. The master curves can be easily converted to families of curves with different mass transfer rates for the same range of perturbation frequencies and compared with experimental data to obtain kinetic information. Examples are given for both PSFR and VSFR systems to demonstrate the ease of application.

It should be understood at the outset that the rate parameters determined by frequency response methods are local values because of the small perturbation involved. Thus, it is possible to develop maps of rate parameter values by varying the concentration and temperature about which the perturbations are performed. This has been done previously[4,8,20,22,31,35,40–45] and permits comparison with theoretical trends predicted by Maxwell-Stefan, Darken, Arrhenius, and other models as well as molecular simulation.

Material and Energy Balances

Depending on the experimental setup, frequency response methods can be divided into two categories: batch systems and flow-through systems. Accordingly, the material and energy balances are different for individual apparatuses. Here, we consider only pure component studies and examine a typical case for each category, pressure-swing FR for the flow-through system and volume-perturbation for the batch system.

Flow-through system

We consider a flow-through system containing an adsorption bed subjected to a periodic (typical sinusoidal) pressure perturbation of frequency ω and amplitude ΔP around the equilibrium state. The flow-rate into the system is maintained constant, and the flow-rate out of the system responds in the periodic state with the same frequency but a different amplitude ΔF. The amplitude ratio ($\Delta F/\Delta P$) of the response relative to the input can be used to extract mass transfer rates from models. The perturbation in pressure is kept small ($<\pm 5\%$) to ensure that the model equations are appropriately linearized. Spherical geometry is assumed here for all of the crystals and pellets, although the particle transfer functions can be replaced by ones with other shape dependencies.

The system volume is modeled between a mass flow controller and a mass-flow meter, as shown in Figure 1. For an ideal gas phase, the material balance can be written

$$M_s \frac{d\hat{n}}{dt} + \frac{V}{RT}\frac{dP}{dt} = F_{in} - F_{out}(t) \tag{1}$$

with[46]

$$\hat{n} = \tilde{n} + (\varepsilon_p/\rho_p)\tilde{c}_p \tag{2}$$

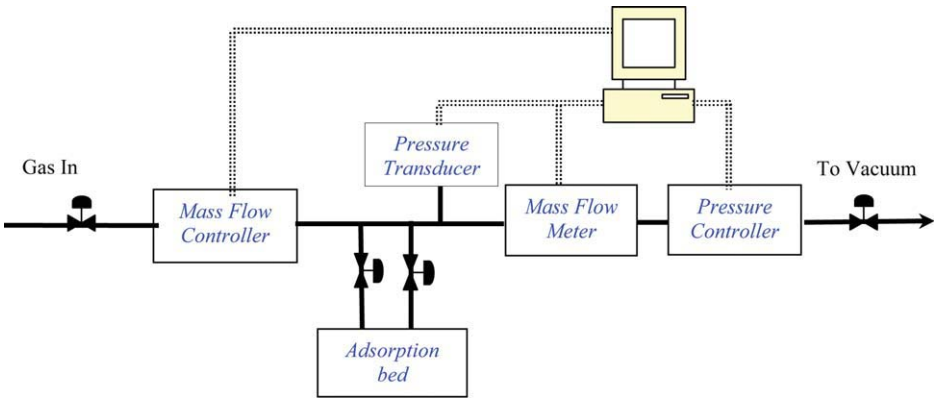

Figure 1. Schematic diagram for PSFR apparatus.

[Color figure can be viewed in the online issue, which is available at wileyonlinelibrary.com.]

where M_s is the mass of the adsorbent, $\hat{n}$ is the total adsorbate concentration in the adsorbent including the average adsorbed-phase concentration $\tilde{n}$ and the average pore fluid concentration in the macropores $\tilde{c}_p$, ε_p is the macropore porosity, ρ_p is the particle density, and V is the extraparticle volume of system. F_{in}, the constant gas molar flowrate into the system, is set by the mass-flow controller. F_{out}, the flow rate leaving through the mass flow meter, is the response variable for pressure perturbation. In writing Eq. 1, consistent with our systems and pressure-swing adsorption processes,[47,48] we have assumed that changes in the molar density of the gas phase due to temperature effects are small compared with those due to pressure effects.

We define the following deviation variables to simplify the material balance

$$n' = n - n_o \tag{3}$$

$$P' = P - P_o \tag{4}$$

$$F' = F_{out} - F_{in} \tag{5}$$

Substituting these into Eq. 1, taking the Laplace transform, combining with the adsorbed-phase transfer function $G_n(s) = \bar{\hat{n}}/\bar{P}$, and simplifying gives the overall transfer function for the apparatus

$$G(s) = \frac{\bar{F}}{\bar{P}} = -s\left[M_s G_n(s) + \frac{V}{RT}\right] \tag{6}$$

By using the common change of variable, $s = j\omega$, we obtain the amplitude ratio divided by frequency from the overall transfer function G

$$\frac{AR}{\omega} = \frac{G(\omega)}{\omega} = \frac{|\bar{F}|}{\omega|\bar{P}|} = \left|M_s G_n(s) + \frac{V}{RT}\right| \tag{7}$$

We typically do not use the phase lag of the transfer function in our analyses as we have found that the values do not change as reliably as amplitude ratio in our experiments.[35] However, the phase lag can easily be obtained from

$$\phi(j\omega) = \tan^{-1}\left[-\frac{M_s\,\mathrm{Re}[G_n(j\omega)] + V/RT}{M_s\,\mathrm{Im}[G_n(j\omega)]}\right] \tag{8}$$

The energy balance is considered in a simple way by adopting the model of Sward and LeVan.[29] They assumed that the bed temperature is uniform and the heat transfer resistance is between the bed and tubing wall. An identical mathematical model can be derived with different parameter values for the case where the heat transfer resistance exists between particles and fluid having the same temperature as the tubing wall. The energy balance for the system is

$$M_s\frac{du_s}{dt} + V\frac{d(cu_f)}{dt} = F_{in}h_{in} - F_{out}h_{out} - hA[T(t) - T_{wall}] \tag{9}$$

where the internal energy u_s for the stationary phase (solid and adsorbate) is[49]

$$u_s = u_{s\,ref} + C_{sol}(T - T_{ref}) + nu_a \tag{10}$$

with $u_a \approx h_a$ for the condensed phase. The enthalpy of the adsorbed phase, h_a, can be evaluated by[49]

$$h_a = h_f + \lambda \tag{11}$$

where the heat of adsorption λ is taken to be negative. For the gas phase, we have

$$h_f = h_{ref} + C_p(T - T_{ref}) \tag{12}$$

$$u_f = h_f - P/c \tag{13}$$

To simplify the energy balance, we multiply Eq. 1 by h_{ref} and subtract it from Eq. 9 to obtain

$$M_s\frac{d(u_s - nh_{ref})}{dt} + V\frac{d(cu_f - ch_{ref})}{dt} = F_{in}(h_{in} - h_{ref}) - F_{out}(h_{out} - h_{ref}) - hA[T(t) - T_{wall}] \tag{14}$$

The change in the energy content of the gas phase is negligible compared with the change in the stationary phase. Thus, the term $d(cu_f - ch_{ref})/dt$ can be discarded. Substituting Eqs. 10 and 11 into Eq. 9 and linearizing, we obtain

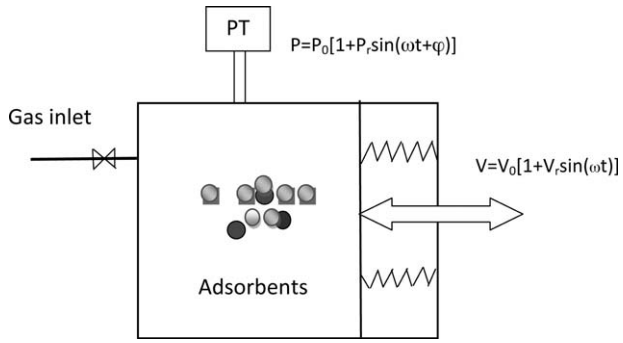

Figure 2. Schematic diagram for VSFR apparatus.

$$M_s C_s \frac{dT'}{dt} - M_s \lambda \frac{dn'}{dt} = -\alpha T'(t) \tag{15}$$

where $C_s = C_{sol} + n_0 C_p$ and $\alpha = F_{in} C_p + hA$. The energy balance transfer function is[29]

$$G_T(s) = \frac{\bar{T}}{\bar{n}} = \frac{M_s \lambda s}{M_s C_s s + \alpha} \tag{16}$$

Batch system

A schematic representation of the VSFR system is shown in Figure 2, where system volume is perturbed periodically around the equilibrium value V_0, and the system pressure P responds accordingly with a phase lag. Assuming an ideal gas, the material balance is

$$M_s \frac{d\hat{n}}{dt} + \frac{d(cV)}{dt} = 0 \tag{17}$$

We use a similar approach as for PSFR to solve Eq. 17 in the Laplace domain. The overall transfer function is

$$G(s) = \frac{\bar{V}}{\bar{P}} = -\left[\frac{V_0}{P_0} + M_s \frac{RT}{P_0} G_n(s)\right] \tag{18}$$

which gives the amplitude ratio

$$\mathrm{AR} = G(w) = \frac{|\bar{V}|}{|\bar{P}|} = \frac{RT}{P_0}\left|M_s G_n + \frac{V_0}{RT}\right| \tag{19}$$

The phase lag is the same as Eq. 8 for PSFR systems.

Dividing both sides of Eq. 19 by RT/P_0, we obtain

$$\frac{\mathrm{AR}}{RT/P_0} = \left|M_s G_n + \frac{V_0}{RT}\right| \tag{20}$$

which has the same right hand side as Eq. 7. Thus, the amplitude ratio curves from the flow-through PSFR and batch VSFR systems are exactly the same once the amplitude ratio curve is defined as $|\bar{F}/\bar{P}|/\omega$ for PSFR and $|\bar{V}/\bar{P}|/(RT/P_0)$ for VSFR. The phase lag curves are also identical for both systems, as given in Eq. 8. Thus, defined this way, the general response curves are not dependent on the FR technique.

The energy balance for the volumetric perturbation system is

$$M_s \frac{du_s}{dt} + \frac{d(cu_f V)}{dt} = -P\frac{dV}{dt} - hA[T(t) - T_{wall}] \tag{21}$$

Using a similar procedure as for the flow-through system with the change in the energy content of the gas phase assumed to be much smaller than that of the stationary phase, we obtain the linearized energy balance

$$M_s C_s \frac{dT'}{dt} - M_s \lambda \frac{dn'}{dt} = -hAT' \tag{22}$$

which is the same energy balance used in previous papers.[20,50]

The energy balance transfer function can be obtained as

$$G_T(s) = \frac{\bar{T}}{\bar{n}} = \frac{M_s \lambda s}{M_s C_s s + \alpha} \tag{23}$$

where $\alpha = hA$.

When comparing the energy balance transfer functions for the flow-through system (Eq. 16) and the batch system (Eq. 23), we find that these two equations are identical except that the parameter α in the denominators is defined differently. Equation 16 for the flow-through systems has the extra contribution $F_{in} C_p$. Thus, compared with a batch system, temperature variations are smaller for a flow-through system for similar experimental conditions.

In general, we find that both flow-through PSFR and batch VSFR systems have the same form of amplitude ratio curves from material balances and the same form of transfer functions from the energy balances. Thus, the amplitude ratio curves for both isothermal and nonisothermal cases would be identical for both flow-through PSFR and batch VSFR systems and are dependent on the adsorbed-phase transfer function G_n, which can be derived from individual rate equations.

Previous analyses of VSFR follow Yasuda's derivation of in-phase and out-of-phase parts of the response function δ, which is based on a general adsorption-desorption rate equation and obeys the following equations[2]

$$(v_r/p_r)\cos\phi - 1 = K_v\,\delta_{in} \tag{24}$$

$$(v_r/p_r)\sin\phi = K_v\,\delta_{out} \tag{25}$$

where v_r and p_r are relative amplitudes of the volume and pressure variations, ϕ is the phase lag, and K_v is an equilibrium constant related to the adsorption isotherm slope at the equilibrium pressure of the FR experiment, i.e., $K_v = (M_s RT/V_0)(dn/dP)_0$. From the experimental results on amplitude ratio and phase lag, the in-phase and out-of-phase transfer functions can be calculated and compared with theoretical values to give the desired mass transfer rate information. Also, the relative amplitude ratio can be easily obtained from in-phase and out-of-phase functions in Eqs. 24 and 25 and is

$$\frac{|\overline{V_r}|}{|\overline{P_r}|} = \sqrt{(K_v\delta_{in} + 1)^2 + (K_v\delta_{out})^2} \tag{26}$$

Rate Equations

The form of the adsorbed-phase transfer function G_n depends on the controlling mass transfer resistances within the particle. An idealized version of the structure of a bidisperse particle is shown in Figure 3. The particle has a radius R_p and is composed of many spherical microporous domains of radius r_s in which adsorption occurs. Mass transfer in the particles occurs (1) in the gas phase in the macropore space, (2) across a pore mouth barrier (if present) at the entrance to the micropore space, and (3) in the adsorbed phase in micropores. To discriminate between the micropore and macropore regions, R is used for the distance along the macropore region and r for the distance along the micropore region. The corresponding nondimensional variables are x_p and x, which are defined as $x_p = R/R_p$ and $x = r/r_s$. For the isothermal case, we consider several different mass transfer models, including the linear driving force (LDF), micropore diffusion, micropore diffusion with surface barrier (such as exists in a carbon molecular sieve), macropore diffusion, and micro-macropore combined resistance with and without a surface barrier resistance. Two nonisothermal cases for LDF and micropore diffusion will be considered. G_n will be derived in the following sections and substituted into the transfer function G (Eq. 7 or 20) to give the amplitude ratio for analysis of mass transfer mechanisms and rates.

For the pure component study, we consider the mechanism of macropore diffusion to be mainly Knudsen diffusion, for which the Knudsen number K_n, defined as the ratio of mean free path to diameter of channel, is close to or much larger than unity.[51] At room temperature and atmospheric pressure, the mean free path for nitrogen is 34 nm, which is the size of a large mesopore. With decreasing pressure, the mean free path increases.

Linear driving force

One of the simplest kinetic models is the linear driving force,[52] for which the mass transfer rate is proportional to how far the adsorbed phase is away from equilibrium. This model can be used to describe the surface barrier resistance at the pore mouth of the micropore region.[6,7,53] The LDF model is expressed by

$$\frac{dn}{dt} = k(n^* - n) \tag{27}$$

where n^* is the adsorbed-phase concentration that would exist in equilibrium with the fluid-phase concentration surrounding the micropore region. The isotherm is linearized about the equilibrium point as the perturbation is very small. Thus, we have

$$n^* - n_0 = K(c - c_0) \tag{28}$$

where K is the local slope of the isotherm. Taking the Laplace transform and solving Eq. 27 for the adsorbed-phase concentration n in micropores gives

$$\bar{n} = \frac{k\bar{n}^*}{s + k} \tag{29}$$

The average amount of sorbate contained in the biporous material, $\hat{\bar{n}}$, is given by

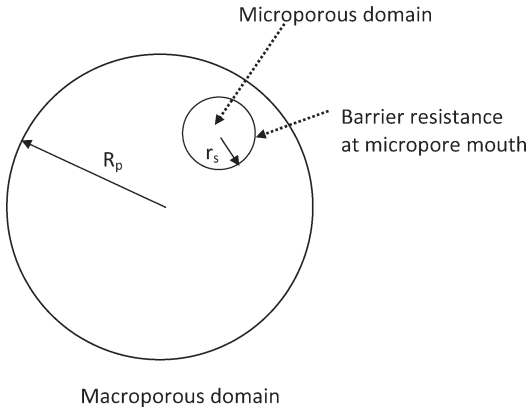

Figure 3. Idealized representation of bidisperse materials.

Macroporous domain showing one of many microporous domains.

$$\hat{\bar{n}}(s) = 3\int_0^1 \left[3\int_0^1 x^2 \bar{n} dx + (\varepsilon_p/\rho_p)\bar{c}\right] x_p^2 dx_p = \left(\frac{kK}{s+k} + \frac{\varepsilon_p}{\rho_p}\right)\bar{c} \tag{30}$$

Thus, the adsorbed-phase transfer function G_n is given by

$$G_n(s) = \frac{\hat{\bar{n}}}{\bar{P}} = \frac{Kk}{RT(s+k)} + \frac{\varepsilon_p}{\rho_p RT} \tag{31}$$

Micropore diffusion

If micropore diffusion (MD) (or surface diffusion) is the rate limiting step, then the rate law in spherical geometry is

$$\frac{\partial n}{\partial t} = \frac{D_s}{r^2}\frac{\partial}{\partial r}\left(r^2 \frac{\partial n}{\partial r}\right) \tag{32}$$

$$n = n^* \quad \text{at} \quad r = r_s \tag{33}$$

$$\frac{\partial n}{\partial r} = 0 \quad \text{at} \quad r = 0 \tag{34}$$

Note that a constant diffusion coefficient has been assumed, which is justified for this linearized system. The solution for this rate equation is given in the Laplace domain as

$$\bar{n}(s,x) = \frac{\bar{n}^*}{x}\frac{\sinh(x\sqrt{s/\eta})}{\sinh(\sqrt{s/\eta})} \tag{35}$$

where $x = r/r_s$ and $\eta = D_s/r_s^2$. We obtain the average loading by integrating over the micropore region to give

$$\tilde{\bar{n}}(s) = 3\int_0^1 \bar{n}(s,x)x^2 dx = 3\frac{\bar{n}^*}{s/\eta}\left[\sqrt{s/\eta}\,\coth(\sqrt{s/\eta}) - 1\right] \tag{36}$$

Considering adsorbate changes in both micropore and macropore regions, for the linearized isotherm, the adsorbed phase transfer function for biporous pellets is given by

$$G_n(s) = \frac{\hat{\bar{n}}}{\bar{P}} = \frac{3K}{RTs/\eta}\left[\sqrt{s/\eta}\coth(\sqrt{s/\eta}) - 1\right] + \frac{\varepsilon_p}{\rho_p RT} \quad (37)$$

Micropore diffusion with barrier resistance

If the constrictions at the microparticle surface (i.e., the pore mouth) cannot be neglected compared with the micropore diffusion resistance, we need a model that allows for a simultaneous existence of micropore diffusion and surface barrier resistances. The governing equation for the distribution of adsorbate is Eq. 32, and the boundary condition imposed at the microparticle surface is

$$D\left.\frac{\partial n}{\partial r}\right|_{r=r_s} = k_b(n^* - n)|_{r=r_s} \quad (38)$$

where k_b is the barrier resistance coefficient in m/s, and r_s is the crystal radius. Using the Laplace transform method to solve Eqs. 9, 11, and 15 for the adsorbed phase concentration, we obtain

$$\bar{n}(s,x) = \frac{\beta\bar{n}^*}{x}\frac{\sinh(x\sqrt{s/\eta})}{(\beta_{bm}-1)\sinh(\sqrt{s/\eta}) + \sqrt{s/\eta}\,\cosh(\sqrt{s/\eta})} \quad (39)$$

where $\beta_{bm} = k_b r_s/D_s$, which is the ratio of the micropore diffusion time scale to the surface barrier time scale. A large value of β_{bm} implies that the system can attain equilibrium rapidly at the micropore mouth.[6] This model reduces to the micropore diffusion model when β_{bm} approaches infinity or the LDF model when β_{bm} approaches zero. Integrating for the average concentration in a biporous adsorbent, we obtain the adsorbed-phase transfer function

$$G_n(s) = \frac{\hat{\bar{n}}}{\bar{P}} = \frac{3K\beta_{bm}}{RT\,s/\eta}\frac{\sqrt{s/\eta}\coth(\sqrt{s/\eta}) - 1}{\sqrt{s/\eta}\coth(\sqrt{s/\eta}) + \beta_{bm} - 1} + \frac{\varepsilon_p}{\rho_p RT} \quad (40)$$

Macropore diffusion

For adsorption in micropores with the mass-transfer resistance in the connecting macropores, the rate equation is

$$\rho_p\frac{\partial n}{\partial t} + \varepsilon_p\frac{\partial c_p}{\partial t} = \frac{\varepsilon_p D_p}{R^2}\frac{\partial}{\partial R}\left(R^2\frac{\partial c_p}{\partial R}\right) \quad (41)$$

$$c_p = c \quad \text{at} \quad R = R_p \quad (42)$$

$$\frac{\partial c_p}{\partial R} = 0 \quad \text{at} \quad R = 0 \quad (43)$$

If adsorption occurs immediately, then the adsorbed-phase concentration is always in equilibrium with the pore concentration, i.e., $n' = Kc'_p$. In terms of the nondimensional variable x_p, we obtain

$$\frac{\partial c_p}{\partial t} = \frac{D_p/R_p^2}{\rho_p K/\varepsilon_p + 1}\frac{1}{x_p^2}\frac{\partial}{\partial x_p}\left(x_p^2\frac{\partial c_p}{\partial x_p}\right) \quad (44)$$

Note that this equation has a similar mathematical form to the micropore diffusion model. Thus, the analytical solution for the macropore diffusion equation is similar to the result for micropore diffusion given by Eq. 35. The average adsorbed amount including adsorbate in both the micropores and macropores is

$$\begin{aligned}\tilde{\bar{n}}(s) &= 3\int_0^1 (\bar{n}(s,x_p) + \varepsilon_p/\rho_p\bar{c}_p(s,x_p))x_p^2 dx_p \\ &= 3(K + \varepsilon_p/\rho_p)\int_0^1 \bar{c}_p x_p^2 dx_p \\ &= \frac{3(K+\varepsilon_p/\rho_p)\bar{c}}{s/\eta_M}(\sqrt{s/\eta_M}\coth(\sqrt{s/\eta_M}) - 1)\end{aligned} \quad (45)$$

where $\eta_M = (D_p/R_p^2)/(\rho_p K/\varepsilon_p + 1)$. The adsorbed phase transfer function is

$$G_n(s) = \frac{\hat{\bar{n}}}{\bar{P}} = \frac{3(K+\varepsilon_p/\rho_p)}{RTs/\eta_M}(\sqrt{s/\eta_M}\coth(\sqrt{s/\eta_M}) - 1) \quad (46)$$

Combined macropore and micropore diffusion

For bidisperse materials, diffusion resistances exist in series for the macropore and micropore regions. The rate equations include two parts, one for micropores:

$$\frac{\partial n}{\partial t} = \frac{D_s}{r^2}\frac{\partial}{\partial r}\left(r^2\frac{\partial n}{\partial r}\right) \quad (47)$$

$$\left.\frac{\partial n}{\partial r}\right|_{r=0} = 0 \quad (48)$$

$$n|_{r=r_s} = n^*(c_p) = Kc_p \quad (49)$$

and another for macropores:

$$\rho\frac{\partial\bar{n}}{\partial t} + \varepsilon_p\frac{\partial c_p}{\partial t} = \frac{\varepsilon_p D_p}{R^2}\frac{\partial}{\partial R}\left(R^2\frac{\partial c_p}{\partial R}\right) \quad (50)$$

$$\left.\frac{\partial c_p}{\partial R}\right|_{R=0} = 0 \quad (51)$$

$$c_p|_{R=R_p} = c \quad (52)$$

The solution for the adsorbed-phase concentration $\bar{n}$ in micropores is given by Eq. 35. The flux leaving the micropore region is

$$\frac{\partial\bar{n}}{\partial t} = \frac{3D_s}{r_s}\left.\frac{\partial n}{\partial r}\right|_{r=r_s} = \frac{3D_s n^*}{r_s}\frac{\sqrt{s/\eta}\cosh(\sqrt{s/\eta}) - \sinh(\sqrt{s/\eta})}{\sinh(\sqrt{s/\eta})} \quad (53)$$

Substituting Eqs. 35 and 53 into Eq. 50 and taking the Laplace transform gives

$$\eta_m\bar{c}_p = \frac{1}{x_p^2}\frac{\partial}{\partial x_p}\left(x_p^2\frac{\partial\bar{c}_p}{\partial x_p}\right) \quad (54)$$

where

$$\begin{aligned}\eta_m &= 3\frac{\rho K}{\varepsilon_p}\frac{D_s/r_s^2}{D_p/R_p^2}\left[\sqrt{s/\eta}\,\coth(\sqrt{s/\eta}) - 1)\right] + \frac{s}{D_p/R_p^2} \\ &= 3\beta_{mM}\left[\sqrt{s/\eta}\,\coth(\sqrt{s/\eta}) - 1)\right] + \frac{\varepsilon_p\beta_{mM}}{\rho_p K}\frac{s}{\eta}\end{aligned} \quad (55)$$

with $\beta_{mM} = (\rho_p K D_s/r_s^2)/(\varepsilon_p D_p/R_p^2)$. Applying the boundary conditions, Eqs. 51 and 52, gives the general solution

$$\bar{c}_p(s,x_p) = \frac{\bar{c}}{x_p}\frac{\sinh(\sqrt{\eta_m}x_p)}{\sinh(\sqrt{\eta_m})} \tag{56}$$

The total amount of sorbate contained in the biporous material, $\hat{n}$, is given by

$$\hat{\bar{n}}(s) = 3\int_0^1 \left[\left(3\int_0^1 \bar{n}(s,x,x_p)x^2dx + \varepsilon_p/\rho_p\right)\bar{c}_p(s,x_p)\right] \times x_p^2 dx_p = 3l_1l_2\bar{c} \tag{57}$$

where

$$l_1 = \frac{\sqrt{\eta_m}\coth(\sqrt{\eta_m}) - 1}{\eta_m} \tag{58}$$

$$l_2 = \frac{3K}{s/\eta}\left[\sqrt{s/\eta}\,\coth(\sqrt{s/\eta}) - 1\right] + \frac{\varepsilon_p}{\rho_p} \tag{59}$$

The adsorbed-phase transfer function for this case is

$$G_n(s) = \frac{\hat{\bar{n}}}{\bar{P}} = \frac{3l_1l_2}{RT} \tag{60}$$

Combined macropore and micropore diffusion with barrier resistance

With consideration of a barrier resistance existing at the external surface of the microporous domain, the boundary condition given by Eq. 49 is replaced by Eq. 38. Solving Eqs. 47–51 and 38 gives

$$G_n(s) = \frac{\hat{\bar{n}}}{\bar{P}} = \frac{3l_1l_2'}{RT} \tag{61}$$

$$l_2' = \frac{3\beta_{bm}K}{s/\eta}\frac{\sqrt{s/\eta}\,\coth(\sqrt{s/\eta}) - 1}{\sqrt{s/\eta}\,\coth(\sqrt{s/\eta}) + \beta_{bm} - 1} + \frac{\varepsilon_p}{\rho_p} \tag{62}$$

This is a general model that can be mathematically reduced to previous models depending on the limits of β_{bm} and β_{mM}. This is shown for all cases in the Appendix.

Nonisothermal LDF and micropore diffusion

Even though our flow-through experimental condition mitigates heat effects compared with traditional batch experiments, the thermal effect can be an important factor in determining rate parameters. With large isosteric heats and slow heat transfer, ignoring the thermal effects may lead to erroneous results.

Because the frequency response methods use only small perturbations to the system, the adsorption equilibrium can be considered linear about the initial steady state, giving

$$n^* = n^*(P_0,T_0) + K(c - c_0) + K_T(T - T_0) \tag{63}$$

where K and K_T are the slopes of the isotherm and isobar, respectively. They are related through the Clausius-Clapeyron type equation[29]

$$K_T = K\lambda\frac{P}{R^2T^3} \tag{64}$$

Substituting Eq. 16 or 23 into the linearized isotherm (Eq. 63), putting the resulting equation into deviation variable form, and taking the Laplace transform gives

$$\bar{n}^* = K\bar{c} + K_T G_T(s)\bar{n} \tag{65}$$

With knowledge of the temperature interference on loadings, we can combine Eq. 65 with adsorbed-phase material balances to obtain the related transfer functions under nonisothermal conditions. For example, substituting Eq. 65 into Eq. 27 gives the nonisothermal LDF transfer function

$$G_n(s) = \frac{\hat{\bar{n}}}{\bar{P}} = \frac{K}{RT\{s/k + 1 + [K_T M_s\lambda/(M_sC_s + \alpha/s)]\}} + \frac{\varepsilon_p}{\rho_p RT} \tag{66}$$

with α being different for flow-through systems and batch systems, defined as $F_{in}C_p + hA$ and hA, respectively. Substituting Eq. 65 into Eq. 36, gives the nonisothermal micropore diffusion transfer function[29]

$$G_n(s) = \frac{\hat{\bar{n}}}{\bar{P}} = \frac{3Kl_3}{RT[1 + 3l_3(K_T M_s\lambda s)/(M_sC_s s + \alpha)]} + \frac{\varepsilon_p}{\rho_p RT} \tag{67}$$

with

$$l_3 = (\eta/s)\left(\sqrt{s/\eta}\coth(\sqrt{s/\eta}) - 1\right) \tag{68}$$

Typically, one or two of the internal rate processes controls the mass transfer rate. We define the mass transfer parameter as p for the main resistance, and the other resistances can be expressed through the relative ratio β compared with the main resistance. The five independent models for isothermal conditions derived above are summarized in Table 1 with the transfer function G_n and related mass transfer parameters p and β.

Exact Solutions

Generally, substituting adsorbed-phase functions listed in Table 1 into the overall transfer functions (Eq. 7 or 20) and calculating the modulus with mathematical symbolic manipulation software can give the amplitude ratio curves. For some simple cases, such as isothermal LDF, micropore, and macropore diffusion, the analytical solutions are quite simple. These are listed in Table 2. The related mass transfer parameters can be directly fitted from the solutions.

Simulation Results and Discussion

The FR methods have the capability of extracting accurate information for mass transfer mechanisms. Depending on the relative time scales of the perturbation and the system intrinsic rate, the corresponding responses vary between two limiting cases: adsorption equilibrium attained (with a much

Table 1. Adsorbed-Phase Transfer Function for Spherical Bidisperse Pellets

Model	$G_n(s) = \hat{\bar{n}}/\bar{P}$	p	β
Iso: LDF	$\dfrac{K}{RT(s/p+1)} + \dfrac{\varepsilon_p}{\rho_p RT}$	k	N/A
Iso: miD	$\dfrac{3K}{RT\, s/p}[\sqrt{s/p}\coth(\sqrt{s/p}) - 1] + \dfrac{\varepsilon_p}{\rho_p RT}$	$\dfrac{D_s}{r_s^2}$	N/A
Iso: miD+barrier	$\dfrac{3K\beta}{RTs/p}\dfrac{\sqrt{s/p}\,\coth(\sqrt{s/p}) - 1}{\sqrt{s/p}\,\coth(\sqrt{s/p}) + \beta - 1} + \dfrac{\varepsilon_p}{\rho_p RT}$	$\dfrac{D_s}{r_s^2}$	$k_b r_s/D_s$
Iso: MaD	$\dfrac{3(K+\varepsilon_p/\rho_p)}{RT\, s/p}(\sqrt{s/p}\,\coth(\sqrt{s/p}\,) - 1)$	$\dfrac{D_p/R_p^2}{\rho_p K/\varepsilon_p + 1}$	N/A
Iso: miD + MaD	$\dfrac{3}{RT}\dfrac{\sqrt{\eta_m}\coth(\sqrt{\eta_m}) - 1}{\eta_m}\left\{\dfrac{3K}{s/p}[\sqrt{s/p}\,\coth(\sqrt{s/p}) - 1] + \dfrac{\varepsilon_p}{\rho_p}\right\}$ $\eta_m = 3\beta[\coth(\sqrt{s/p})\sqrt{s/p} - 1)] + \dfrac{\varepsilon_p\beta}{\rho_p K}\dfrac{s}{p}$	$\dfrac{D_s}{r_s^2}$	$\dfrac{\rho_p K}{\varepsilon_p}\dfrac{D_s/r_s^2}{D_p/R_p^2}$
Iso: miD + barrier + MaD	$\dfrac{3}{RT}\dfrac{\sqrt{\eta_m}\coth(\sqrt{\eta_m}) - 1}{\eta_m}\left\{\dfrac{3\beta_{bm}K}{s/p}\dfrac{\sqrt{s/p}\,\coth(\sqrt{s/p}) - 1}{\sqrt{s/p}\,\coth(\sqrt{s/p}) + \beta_{bm} - 1} + \dfrac{\varepsilon_p}{\rho_p}\right\}$ $\eta_m = 3\beta[\coth(\sqrt{s/p})\sqrt{s/p} - 1)] + \dfrac{\varepsilon_p\beta}{\rho_p K}\dfrac{s}{p};\ \beta_{bm} = k_b r_s/D_s$	$\dfrac{D_s}{r_s^2}$	$\dfrac{\rho_p K}{\varepsilon_p}\dfrac{D_s/r_s^2}{D_p/R_p^2}$
Noniso: LDF	$\dfrac{K}{RT[s/p + 1 + K_T M_s\lambda/(M_s C_s + \beta p/s)]} + \dfrac{\varepsilon_p}{\rho_p RT}$	k	$\dfrac{\alpha}{k}$
Noniso: miD	$\dfrac{3Kl_3}{RT[1 + 3l_3(K_T M_s\lambda)/(M_s C_s + \beta p/s)]} + \dfrac{\varepsilon_p}{\rho_p RT}$ $l_3 = (p/s)\left(\sqrt{s/p}\,\coth(\sqrt{s/p}) - 1\right)$	$\dfrac{D_s}{r_s^2}$	$\dfrac{\alpha}{D_s/r_s^2}$

larger perturbation time scale compared with the system mass transfer time scale) and essentially no adsorption occurring (with a very short perturbation time scale compared with the system mass transfer time scale).

To understand how systems respond to the mass transfer resistances, we study a series of mass transfer resistances theoretically, including individual resistances and their combinations, and we predict the corresponding response curves as a function of the relative ratio of perturbation frequencies to mass transfer rates within the range 10^{-3} to 10^5. We consider an example case with system parameters given in Table 3.

Figure 4a shows characteristic master response curves for different mass transfer resistances for five isothermal cases and two nonisothermal cases. The x-axis is the ratio of perturbation frequency to the mass transfer parameter p, which is defined differently depending on the model as shown in Table 1. The y-axis depends on the type of system with values corresponding to the modulus of $|M_s G_n + V/(RT)|$. For PSFR, it is the amplitude ratio $|\bar{F}/\bar{P}|$ divided by the frequency, based on Eq. 7. For VSFR, it is the amplitude ratio $|\bar{V}/\bar{P}|$ divided by RT/P_0, based on Eq. 20. The corresponding phase shift plot is shown in Figure 4b.

Depending on the adsorbed-phase transfer function G_n, the response curves give distinctive differences for various kinetic regimes. For a system having no adsorption on inert, non-porous material (e.g., glass beads), the y-axis gives extraparticle volume information, i.e., $V/(RT)$. It is represented by the low dotted line in Figure 4a. For the limiting situation of slow cycling, systems show the full equilibrium capacity of the adsorbent to capture gases as represented by the slope of the isotherm at the perturbation. From the plot, all of the response ratio curves approach the value $[(M_s(\varepsilon_p/\rho_p + K) + V)/RT]$ asymptotically for a relative ratio of ω/p less than 0.001. This means that systems stay near equilibrium continuously if the perturbation time scale is 1000 times

Table 2. Exact Solutions for Amplitude Ratio Curves

Model	Amplitude Ratio PSFR: $\lvert F\rvert/(\omega\lvert P\rvert)$; VSFR: $(\lvert V/P\rvert/(RT/P_0)$
Iso: LDF	$\sqrt{\left(\dfrac{M_s\omega kK/(RT)}{\omega^2 + k^2}\right)^2 + \left(\dfrac{M_s k^2 K/(RT)}{\omega^2 + k^2} + \dfrac{M_s\varepsilon_p}{\rho_p RT} + \dfrac{V}{RT}\right)^2}$
Iso: miD	$\sqrt{\left[M_s\dfrac{6K}{RTv^2}\left(\dfrac{v}{2}\dfrac{\sinh v + \sin v}{\cosh v - \cos v} - 1\right)\right]^2 + \left[M_s\dfrac{3K}{vRT}\dfrac{\sinh v - \sin v}{\cosh v - \cos v} + \dfrac{M_s\varepsilon_p}{\rho_p RT} + \dfrac{V}{RT}\right]^2}$ $v = \sqrt{2\omega/(D_s/r_s^2)}$
Iso: MaD	$\sqrt{\left[M_s\dfrac{6(K+\varepsilon_p/\rho_p)}{RTv^2}\left(\dfrac{v}{2}\dfrac{\sinh v + \sin v}{\cosh v - \cos v} - 1\right)\right]^2 + \left[M_s\dfrac{3(K+\varepsilon_p/\rho_p)}{vRT}\dfrac{\sinh v - \sin v}{\cosh v - \cos v} + \dfrac{V}{RT}\right]^2}$ $v = \sqrt{2\omega(K\rho_p/\varepsilon_p + 1)/(D_p/R_p^2)}$

Table 3. System Properties Used in Theoretical Study

System pressure (P)	1 bar
System volume (V)	4.2×10^{-5} m^3
Temperature (T)	298.15 K
Isotherm slope	1 mol/(kg bar)
Particle density (ρ_p)	760 kg/m^3
Adsorbent mass (M_s)	0.002 kg
Macropore porosity (ε_p)	0.43

larger than the system mass transfer time scale. The difference between this asymptote and the flat response curve of no adsorption is comprised of two parts, gas adsorbed in micropores [$M_sK/(RT)$] and gas stored in macropores [$M_s\varepsilon_p/(\rho_p/RT)$]. Generally, the contribution from gas storage in macropores is much smaller than that from adsorption in micropores. For the example in the simulation, only 1.2% of the capacity is in macropores. The difference between two the response curves of adsorbate and inert gas gives the ability to obtain the equilibrium capacities for the system without requiring additional isotherm measurements.[35]

For another limiting situation, with the perturbation time scale much smaller than the time scale for mass transfer, the amplitude ratio curves approach a plateau with essentially no adsorption occurring. Depending on the mass transfer mechanisms, the plateaus can be different. For mass transfer resistances only existing in micropore regions, the gas in both the adsorbent macropores and the system volume can follow the very fast perturbation. Thus, the value of plateau includes both accessible macropore volume [$M_s\varepsilon_p/(\rho_pRT)$] and the system external volume [$V/(RT)$]. However, with mass-transfer resistances existing in both macropore and micropore regions, the gas can only follow the fast perturbation in the system volume [$V/(RT)$]. Then, the amplitude ratio curves approach the response curve on an inert, nonporous material. It is apparent that the minimum relative rate ratio (ω/p) is above 10 for this situation. However, this relative ratio can be somewhat different depending on the controlling mass-transfer mechanism.

Except for these two limiting situations of all response curves having the same asymptotes, the response curves from diverse mass-transfer mechanisms exhibit distinctive shapes. It is clear from Figure 4a that the nonisothermal and isothermal cases are easily separated. The two nonisothermal cases, nonisothermal LDF, and nonisothermal MD show heat interference in the low x-axis range. The curves have an extra step compared with their relative isothermal models. Also, two peaks are shown in the phase lag plot, Figure 4b, for the nonisothermal model. This can be explained by the coupling between heat and mass transfer to decrease the mass uptake due to the temperature rise inhibiting adsorption once pressure is increased, and the temperature drop reducing desorption once the pressure is decreased. With increasing pressure perturbation frequency, the nonisothermal models approach isothermal models as the differential quantity adsorbed approaches zero.

The micropore diffusion model with a mass-transfer parameter of D_s/r_s^2 and the macropore diffusion model with a mass transfer parameter of $D_p/R_p^2/(\rho_pK/\varepsilon_p + 1)$ are similar as shown in Figure 4a. Both response curves have a long tail between two asymptotes. The similarity is caused by their analogous mathematical forms. The only difference is in the asymptote for fast perturbation where the micropore model shows a slightly higher asymptote compared with the macropore model because of gas cycling in macropores.

For mass-transfer resistances in series, such as the micropore with barrier resistance model and the combined macropore and micropore resistance model, the response curves move slightly to the left compared with individual mass transfer resistances. This implies slower apparent mass-transfer rates for the system caused by the extra mass-transfer steps, as would be expected.

For systems with complicated mass-transfer resistances, such as multiple mass transfer steps in series or combined

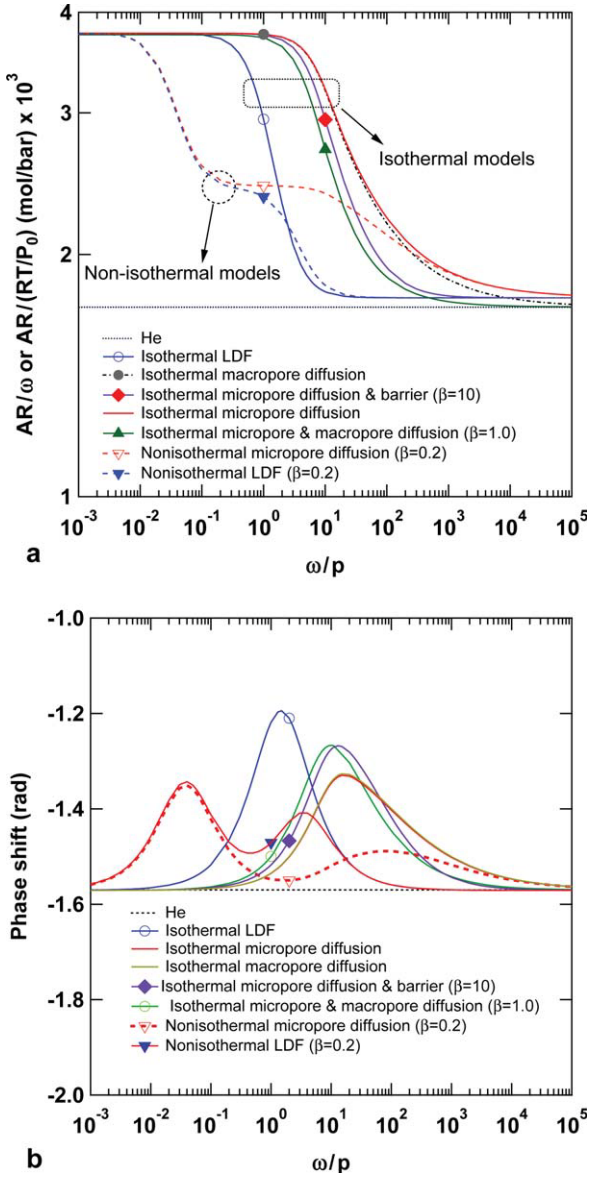

Figure 4. Comparison of characteristic curves from different mass transfer resistances.

(a) Amplitude ratio response curves, $|\bar{F}/\bar{P}|/\omega$ for PSFR by Eq. 7 and $|\bar{V}/\bar{P}|/(RT/P_0)$ for VSFR by Eq. 20; (b) phase lag response curves. [Color figure can be viewed in the online issue, which is available at wileyonlinelibrary.com.]

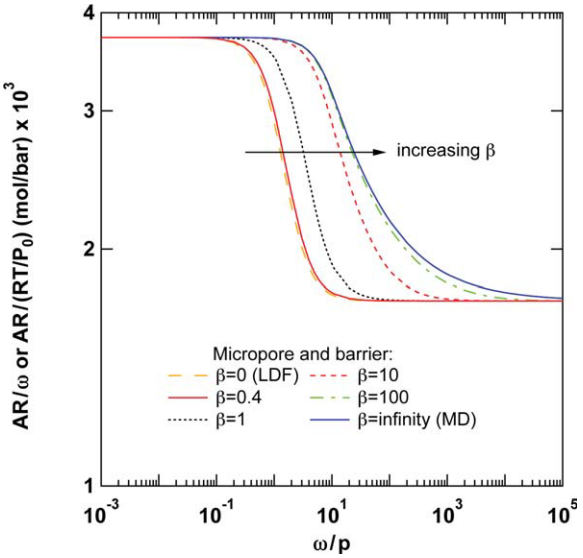

Figure 5. Effect of barrier resistance on characteristic response curves.

[Color figure can be viewed in the online issue, which is available at wileyonlinelibrary.com.]

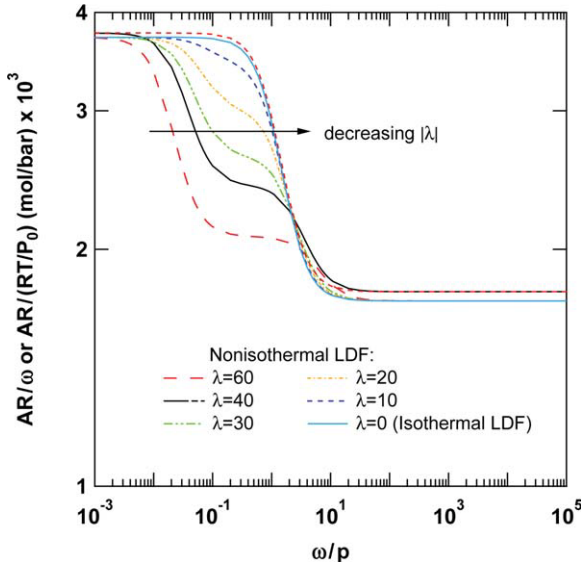

Figure 6. Effect of isosteric heat on characteristic response curves.

[Color figure can be viewed in the online issue, which is available at wileyonlinelibrary.com.]

mass and heat transfer resistances, the response curves are dependent on more than one mass transfer rate parameter. Figure 5 shows the response curves for the combined micropore and barrier resistance model. The value of β gives the relative ratio of the surface barrier and micropore diffusion time scales. A small value of β is characteristic of a dominant surface barrier resistance. With β decreasing from 10 to 1, the characteristic curve from the combined micropore and surface barrier resistance model moves close to that of the LDF model. On the contrary, with β increasing from 10 to 100, the time scale of the barrier resistance reduces to 100 times less than that for micropore diffusion, and the characteristic curve for the combined micropore and surface barrier resistance model moves close to that from the MD model, which does not consider any surface barrier resistance.

For nonisothermal cases, the response curves are also related with the heat-transfer coefficient α and isosteric heat λ. With an increasing isosteric heat or a decreasing heat transfer coefficient, the heat interference becomes strong and causes an obvious step in the response curves, as shown in Figures 6 and 7. For systems with an isosteric heat less than 10 kJ/mol or systems with significantly large effective heat transfer coefficients compared with mass transfer coefficients ($\beta > 100$), the corresponding curves from the nonisothermal model are almost the same as for the isothermal case because no significant temperature variations occur within the system to influence the mass transfer steps. Figures 6 and 7 are shown for the LDF model, and similar trends are observed for the MD model.

A more general model that considers both macropore and micropore resistances combined with a barrier resistance provides a strong basis for analyzing rate information for common biporous materials, such as pelletized zeolites and metal organic frameworks (MOFs). We consider this three resistance model in three ways. First, we investigate the relative importance for the two diffusivities, micropore and macropore. Given the ratio of the micropore and macropore diffusivity terms, $\beta_{mM} = (D_s/r_s^2)(K\rho_p/\varepsilon_p)/(D_p/R_p^2)$, we simulate the response curves by varying one of the diffusivities while holding the other one constant. The results are shown in Figure 8a for a constant micropore diffusivity and in Figure 8b for a constant macropore diffusivity, respectively. From both figures, we find that micropore diffusion becomes dominant when β_{mM} is less than 0.1, and macropore diffusion is dominant when β_{mM} is larger than 100. For systems with an intermediate β_{mM}, both resistances can be important and contribute to the mass transfer process.

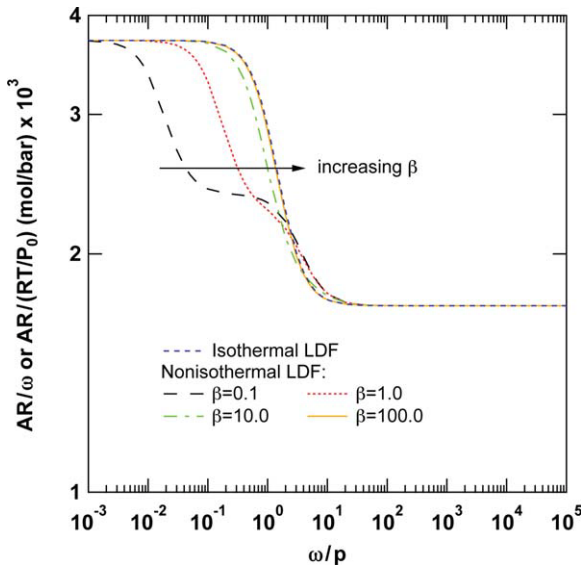

Figure 7. Effect of heat-transfer coefficients on characteristic response curves (λ in kJ/mol).

[Color figure can be viewed in the online issue, which is available at wileyonlinelibrary.com.]

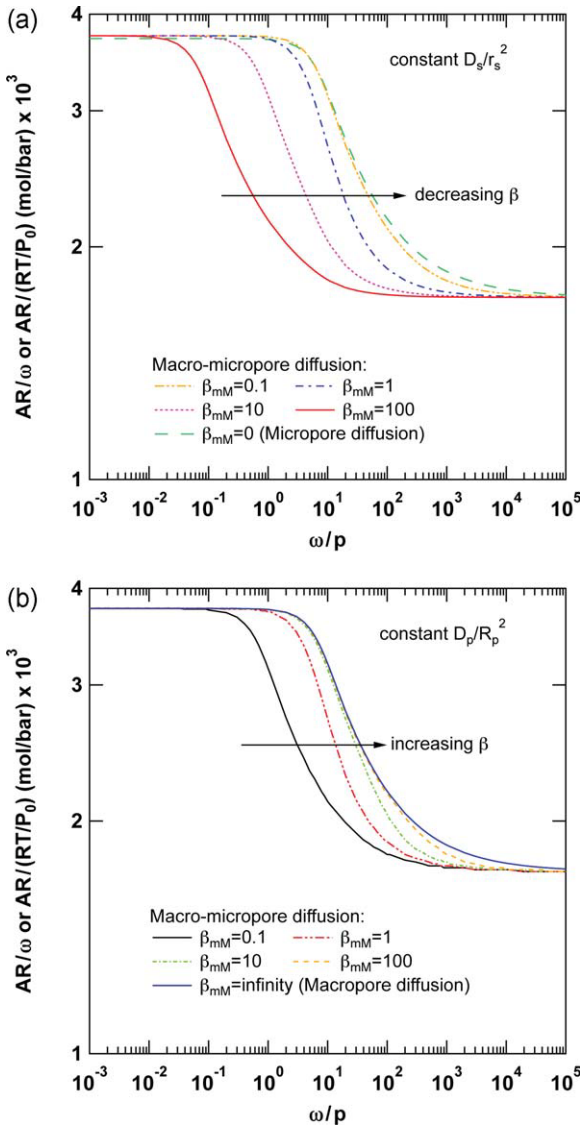

Figure 8. Comparison of relative importance of micropore and macropore diffusivities for combined macropore and micropore diffusion model.

(a) constant micropore diffusivity and (b) constant macropore diffusivity. [Color figure can be viewed in the online issue, which is available at wileyonlinelibrary.com.]

Second, we are interested in how the macropore porosity ε_p affects the system performance. With increasing ε_p, more adsorbate is captured in the macropores, and this contributes to the maximum capacity of the system. Although a small effect, when ε_p is large (e.g., $\varepsilon_p \geq 0.9$ as may exist for an aerogel, xerogel, and possibly some MOFs), it is nevertheless apparent. Figure 9 shows the effect on the equilibrium asymptote.

Lastly, we study multiple resistance effects on the biporous model. The relative importance of a barrier resistance and micropore diffusion is reflected by the value of β_{bm}, and the relative importance of micropore diffusion and macropore diffusion is represented by β_{mM}. In Figure 10, we simulate the response curves with β_{mM} varying while β_{bm} is fixed. For a constant β_{bm}, representing a set relative impor-

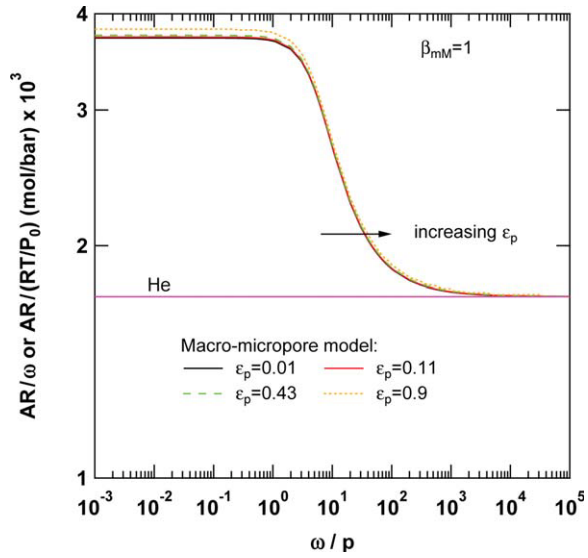

Figure 9. Effect of macropore porosity on combined macropore and micropore diffusion model.

[Color figure can be viewed in the online issue, which is available at wileyonlinelibrary.com.]

tance of barrier and micropore diffusion, increasing β_{mM} results in a strong macropore diffusion resistance. We can see that the curves move to the left, which shows a slower apparent mass transfer rate caused by inclusion of the macropore resistance. With different combinations of these two parameters, β_{bm} and β_{mM}, the master curves show distinct shapes and locations in Figure 10. Jordi and Do[6,7] have carried out an in-depth analysis for the volume perturbation method and show the nondimensionized in-phase and out-phase characteristic transfer functions for slab, cylindrical,

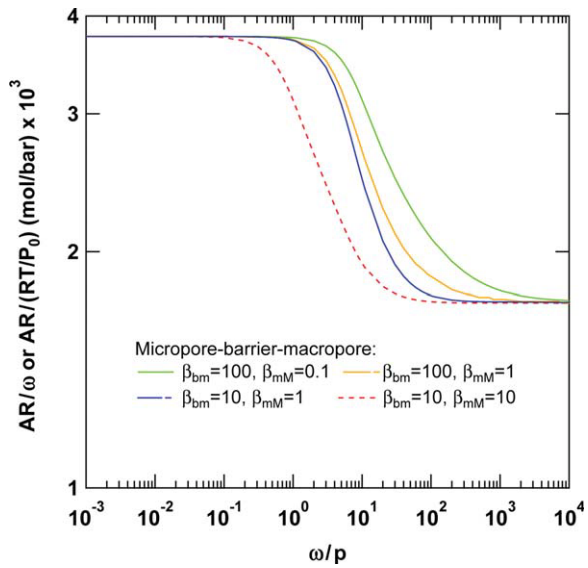

Figure 10. Effect of external film resistance on combined macropore and micropore diffusion model.

[Color figure can be viewed in the online issue, which is available at wileyonlinelibrary.com.]

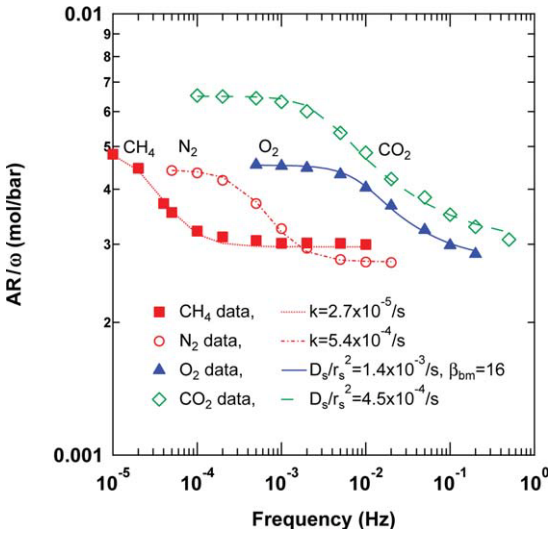

Figure 11. Experimental data and simulation results for N_2, O_2, CH_4, and CO_2 on CMS at 1 atm and 25°C using PSFR.

[Color figure can be viewed in the online issue, which is available at wileyonlinelibrary.com.]

and spherical geometries. Their results show distinct curves, as do ours, for different degenerate models.

Experimental Examples

We have developed the master curves for different mass transfer mechanisms as a function of the ratio of perturbation frequency to system intrinsic rate. From an experimental point of view, we perturb a system around equilibrium at different frequencies, and the system responds depending on its own intrinsic mass transfer rate. Thus, the master curves can be inverted into a smooth family of curves as a function of the rate parameters. In the following, we use published data to demonstrate how to obtain mass transfer rates from the models.

N_2, O_2, CH_4, and CO_2 on CMS

Mass-transfer rates for these four pure components have been measured at 25°C and 1 bar using the PSFR method. Detailed information is given elsewhere.[31,35] Figure 11 shows the experimental data and the best fit for CH_4, N_2, O_2, and CO_2. The two left curves, for CH_4 and N_2, are described well by the LDF model, which accounts for the barrier resistance at the pore mouth of CMS. The right curve for CO_2 is best described by the micropore diffusion model. The response curve for O_2, lying in the middle, is best described by the combined resistance model with micropore diffusion and barrier resistances. The controlling mass-transfer mechanisms are consistent with molecular sizes. Among these four gases, CH_4 has the largest molecular size (~4 Å), and N_2 has the second largest (~3 Å). Thus, the mass-transfer rates of these two molecules is limited by the size of the pore window of the CMS (Takeda 3A). Both O_2 and CO_2 have smaller sizes (~2.8 Å) and less barrier resistance compared with CH_4 and N_2.

Chloroethane on BPL AC

Mass-transfer rates have been measured for adsorption of chloroethane on BPL activated carbon at 25°C and 0.1 atm using the PSFR method.[31] The sample weight was 5.37 g, and V/RT was 0.00295 mol/bar for the experiment. The isotherm slope was 7.77 mol/(kg atm). The experimental data and families of curves are shown in Figure 12. Helium data are shown as open circles horizontally, with the y-axis giving the value of V/RT. The chloroethane data are shown as filled circles with a distinct two-step curve, which indicates heat interference. The data have the same shape as the master curve for nonisothermal micropore diffusion model with a value for β of 9.5. A family of curves with different mass-transfer rates can be developed from the master curve, as shown in Figure 12, with slow rates shown on the left side and fast rates appearing on the right side of the figure. Using nonlinear regression, the intrinsic mass transfer rate is $p = D_s/r_s^2 = 8.1 \times 10^{-3}$/s. Another way to obtain the mass-transfer rate would be to locate the experimental response on the y-axis of the master curve, then read the value of ω/p from the x-axis and calculate p given the experimental frequency.

CO_2 on 5A powder

Onyestyák et al.[54] studied the diffusion of CO_2 on 5A zeolite powder by VSFR. Figure 13a shows the frequency response in-phase and out-of-phase characteristic functions measured at 348 K and 0.0013 atm. We have shown how to obtain the relative amplitude ratio from information on in-phase and out-of-phase characteristic functions using Eq. 26. The relative amplitude ratio curve is shown in Figure 13b with the modulus corresponding to $|(RTM_s/V_0)G_n + 1|$. Using the various expressions for G_n in Table 1, the curve is best described by the combined resistance model of micropore

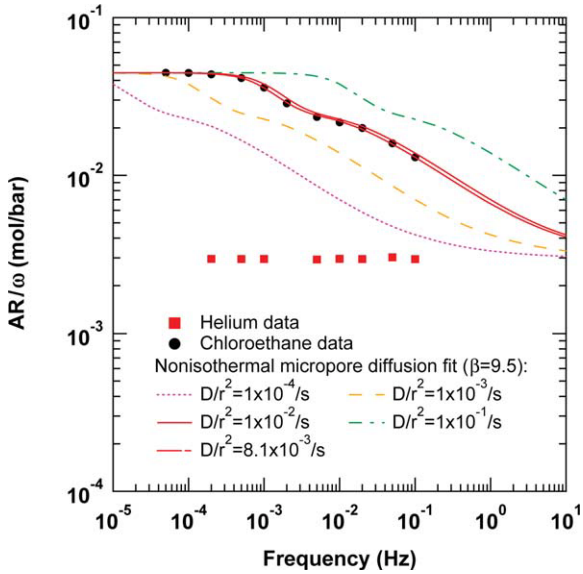

Figure 12. Experimental data and simulation results for chloroethane on BPL AC at 0.1 atm and 25°C using PSFR.

[Color figure can be viewed in the online issue, which is available at wileyonlinelibrary.com.]

diffusion and a barrier resistance with parameter values of $D_s/r_s^2 = 5.5 \times 10^{-2}$/s and $\beta = 8.9$, corresponding to a barrier resistance coefficient of $k_b/r_s = D_s/r_s^2 \times \beta = 0.49$/s. This result is consistent with the findings of Onyestyá et al. They obtained a time constant for diffusion, defined as $1/(D/r^2)$, of ~100 s and a time constant for the barrier resistance of about 0.4 s.

Argon on LSX zeolite

Bülow and Shen[45] used the VSFR method to study adsorption of argon on beads of a lithium-based, rare earth, low silicon, X-type (LSX) zeolite. They obtained in-phase and out-of-phase data, $K_v\delta_{in}$ and $K_v\delta_{out}$, at 273 K and 0.026 atm. These are shown in Figure 14a, where they are described by a diffusion model with an effective time constant of $t_e = 8.29$ s. Using our analysis, the response curve, defined as $|\bar{V}/\bar{P}|/(RT/P_0)$ for the VSFR system, can be easily converted from the reported in-phase and out-of-phase data to the amplitude ratio curve shown in Figure 14b. The data are described by the diffusion model with $D/r^2 = 0.12$/s, which corresponds to a time constant of $t_e = 8.29$ s, which is identical to the value obtained by Bülow and Shen.

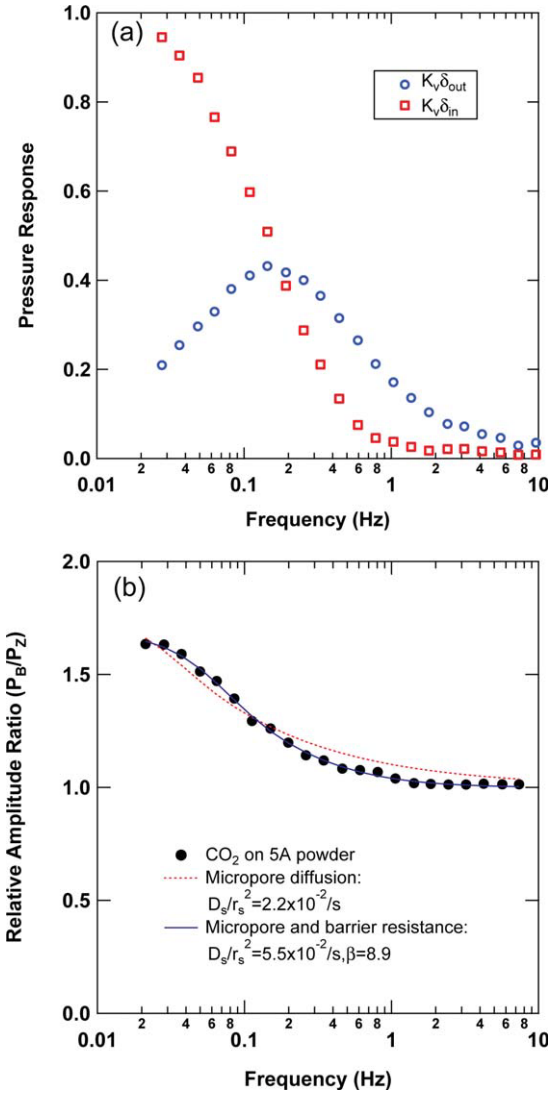

Figure 13. Experimental data and simulation results for CO_2 on Lancaster 5A zeolite powder at 348 K and 0.0013 atm using VSFR.

(a) In-phase $K_v\delta_{in}$ and out-phase $K_v\delta_{out}$ characteristic functions[54]; (b) amplitude ratio curves. [Color figure can be viewed in the online issue, which is available at wiley onlinelibrary.com.]

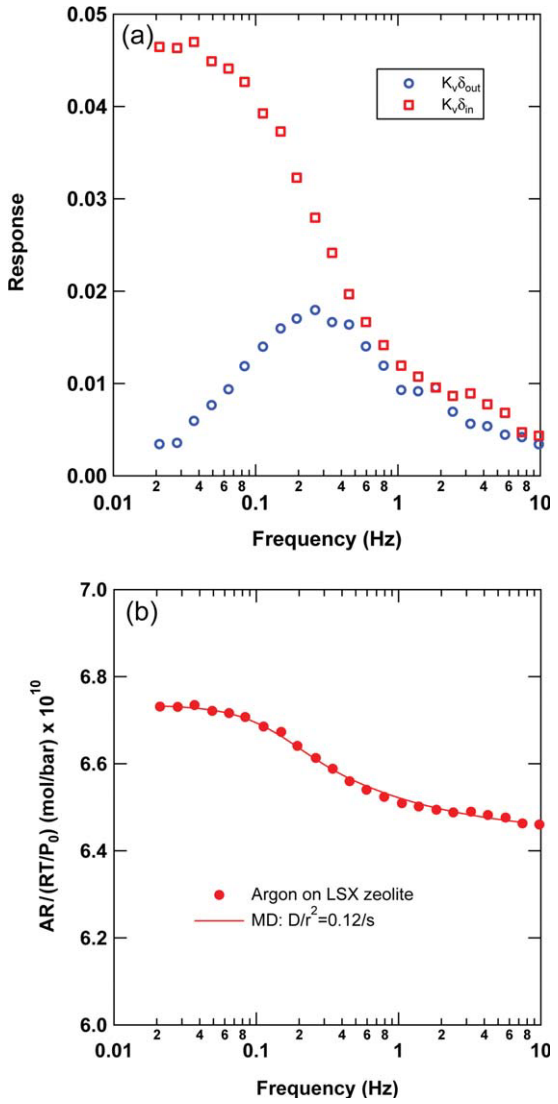

Figure 14. Experimental data and simulation results for argon on LSX zeolite beads at 273 K and 0.026 atm using VSFR.

(a) In-phase $K_v\delta_{in}$ and out-phase $K_v\delta_{out}$ characteristic functions[45]; (b) amplitude ratio curves. [Color figure can be viewed in the online issue, which is available at wiley onlinelibrary.com.]

Conclusions

We have developed a mathematical model and solved it analytically for both flow-through and batch systems. The model considers a variety of mass-transfer resistances acting independently or in combination. Six isothermal solutions have been formulated: linear driving force, micropore

diffusion (surface diffusion), micropore diffusion combined with a barrier resistance, macropore diffusion, and macropore and micropore diffusion with or without a barrier resistance. Heat effects have been considered for two cases, a nonisothermal linear driving force and nonisothermal micropore diffusion, and the related analytical solutions have been developed. We have shown that amplitude ratio information can be represented in a common form for both batch systems subjected to volumetric perturbation and flow-through systems with pressure swings.

Amplitude ratio curves have been simulated and compared for distributed mass-transfer resistances. It is clear that FR can discriminate among different mass-transfer resistances, which are represented by master curves dependent on the relative ratio of perturbation and system intrinsic rates. For nonisothermal cases, response curves have an obvious additional step in comparison with the curves for isothermal models.

Systems with more than one mass transfer resistance can have more complicated response curves depending on the relative ratio of controlling mass transfer resistances. The curve shape changes with the value of β, which represents the relative ratio of micropore diffusion to a barrier resistance, combined macropore to micropore diffusion, and heat to mass transfer coefficients. A large or small value of β implies that one transfer resistance can be neglected. With an intermediate value, the response curve moves to the left in relation to the curve without the extra resistance, which means the system has a slower overall mass transfer rate.

Examples, with pure N_2, O_2, CH_4, and CO_2 adsorbed on CMS and chloroethane adsorbed on BPL activated carbon in PSFR systems and CO_2 adsorbed on 5A powder and argon adsorbed on LSX zeolite beads in VSFR systems, demonstrate how to use the general model and master curves to extract mass transfer mechanisms and rates. The chloroethane data have a two-step shape that is described well by a nonisothermal micropore diffusion model. The master curve easily converts to a family of curves for distinct mass-transfer rates, with slow rates appearing on the left and fast rates appearing on the right. This enables easy determination of mass transfer rates directly from the location of the curves. In-phase and out-of-phase data from VSFR can be easily treated, and the general model can be applied identically to both PSFR and VSFR systems.

Notation

C_s = heat capacity of a solid, J/(kg K)
C_p = heat capacity of an ideal gas, J/(mol K)
c = extraparticle fluid-phase concentration, mol/m^3
c_p = fluid-phase concentration in macropores, mol/m^3
D_s = micropore diffusivity, m^2/s
D_p = macropore diffusivity, m^2/s
F_{in} = constant gas mass flowrate into system, mol/s
F_{out} = gas mass flowrate through mass flow meter, mol/s
G = transfer function for entire system
G_n = transfer function for adsorbed-phase
h = enthalpy, J/mol for fluid phase, J/kg for the stationary phase
hA = heat-transfer parameter, J/(K s)
k = mass transfer coefficient, s^{-1}
k_b = barrier resistance coefficient, m/s
K = local slope of isotherm, m^3/kg
K_T = isobar
K_v = equilibrium constant
M_s = amount of adsorbent, g
l = parameter used in Eqs. 58–62
n = adsorbate concentration in micropore, mol/kg
$\hat{n}$ = total concentration in biporous adsorbent, Eq. 2, mol/kg
P = pressure, bar
r = distance along microparticle radius, m
r_s = microparticle radius, m
R = distance along macroparticle radius, m; ideal gas constant, J/(mol K)
R_p = macroparticle radius, m
s = complex argument in Laplace domain, $s = j\omega$
T = temperature, K
u = internal energy, J/mol for fluid phase, J/kg for stationary phase
V = volume of pressure-controlled region, m^3

Greek letters

α = lumped parameter $[F_{in}C_p + hA]$ or $[hA]$
β = relative ratio parameter
ε_p = macropore porosity
η = parameter $[D_s/r_s^2]$
η_M = parameter $[D_p/R_p^2/(\rho_p K\varepsilon_p + 1)]$
η_m = parameter defined in Eq. 55
θ = fractional coverage of adsorption sites
ω = frequency, Hz
λ = heat of adsorption, kJ/mol
δ = in-phase and out-of-phase response function
ϕ = phase lag
ρ = density, kg/m^3

Superscripts

$'$ = deviation variable
$*$ = equilibrium state
$-$ = Laplace domain

Subscripts

o = equilibrium (mean) state

Literature Cited

1. Sun LM, Meunier F. On the heat effect in measurements of sorption kinetics by the frequency response method. *Chem Eng Sci*. 1993;48:715–722.
2. Yasuda Y. Frequency response method for study of the kinetic behavior of a gas-surface system. 1. Theoretical treatment. *J Phys Chem*. 1976;80:1867–1869.
3. Yasuda Y. Frequency response method for investigation of gas/surface dynamic phenomena. *Heterogen Chem Rev*. 1994;1:103–124.
4. Reyes SC, Iglesia E. Frequency response techniques for the characterization of porous catalytic solids. *Catalysis*. 1994;11:51–92.
5. Reyes SC, Sinfelt JH, DeMartin GJ, Ernst RH. Frequency modulation methods for diffusion and adsorption measurements in porous solids. *J Phys Chem B*. 1997;101:614–622.
6. Jordi RG, Do DD. Analysis of the frequency response method for sorption kinetics in bidispersed structured sorbents. *Chem Eng Sci*. 1993;48:1103–1130.
7. Jordi RG, Do DD. Analysis of the frequency response method applied to non-isothermal sorption studies. *Chem Eng Sci*. 1994;49:957–979.
8. Song LJ, Rees LVC. Adsorption and diffusion of cyclic hydrocarbon in MFI-type zeolites studied by gravimetric and frequency-response techniques. *Micro Meso Mater*. 2000;35–36:301–314.
9. Vlyon J, Onyestyák G, Rees LVC. A frequency-response study of the diffusion and sorption dynamics of ammonia in zeolites. *Langmuir*. 2000;16:1331–1336.
10. Yasuda Y. Frequency response method for study of the kinetic behavior of a gas-surface system. 2. An ethylene-on-zinc oxide system. *J Phys Chem*. 1976;80:1870–1875.
11. Yasuda Y. Determination of vapor diffusion coefficients in zeolite by the frequency response method. *J Phys Chem*. 1982;86:1913–1917.
12. Yasuda Y, Sugasawa G. A frequency response technique to study zeolitic diffusion of gases. *J Catal*. 1984;88:530–534.

13. Yasuda Y, Yamamoto A. Zeolitic diffusivities of hydrocarbons by the frequency response method. *J Catal*. 1985;93:176–181.
14. Yasuda Y. Kinetic details of a gas/porous adsorbent system by the frequency response method. *J Phys Chem*. 1991;95:2486–2492.
15. Yasuda Y. Frequency response method for study of the kinetic details of a heterogeneous catalytic reaction of gases. 1. Theoretical treatment. *J Phys Chem*. 1993;97:3314–3318.
16. Yasuda Y, Nomura K. Frequency response method for study of the kinetic details of a heterogeneous catalytic reaction of gases. 2. A methanol conversion to olefins. *J Phys Chem*. 1993;97:3319–3323.
17. Yasuda Y, Mizusawa H, Kamimura T. Frequency response method for investigation of kinetic details of a heterogeneous catalyzed reaction of gases. *J Phys Chem B*. 2002;106:6706–6712.
18. Yasuda Y, Matsumoto A, Oda R. Reaction rate spectroscopy for a catalyzed reaction of gases. *Bull Chem Soc Jpn*. 2004;77:1973–1986.
19. Van-Den-Begin NG, Rees LVC, Caro J, Bülow M, Hunger M, Kärger J. Diffusion of ethane in silicalite-1 by frequency response, sorption uptake and nuclear magnetic resonance techniques. *J Chem Soc Faraday Trans*. 1989;85:1501–1509.
20. Sun LM, Bourdin V. Measurement of intracrystalline diffusion by the frequency response method: analysis and interpretation of bimodal response curves. *Chem Eng Sci*. 1993;48:3783–3793.
21. Sun LM, Meunier F, Grenier P. Frequency response for nonisothermal adsorption in biporous pellets. *Chem Eng Sci*. 1994;49:373–381.
22. Giermanska KJ, Cartigny J, Lara ECD, Sun LM. Heat effect and intercrystalline diffusion of light *n*-alkanes in zeolite NaX measured by frequency response method. *Zeolites*. 1996;17:365–372.
23. Bourdin V, Grenier P, Meunier F, Sun LM. Thermal frequency response method for the study of mass-transfer kinetics in adsorbents. *AIChE J*. 1996;42:700–712.
24. Boniface HA, Ruthven DM. Chromatographic adsorption with sinusoidal input. *Chem Eng Sci*. 1985;40:2053–2061.
25. Li YE, Willcox D, Gonzalez RD. Determination of rate constants by the frequency response method: CO on Pt/SiO_2. *AIChE J*. 1989; 35:423–428.
26. Kramers H, Alberda G. Frequency response analysis of continuous flow systems. *Chem Eng Sci*. 1953;2:173–181.
27. Park IS, Petkovska M, Do DD. Frequency response of an adsorber with modulation of the inlet molar flow-rate—I. a semi-batch adsorber, II. a continuous flow adsorber. *Chem Eng Sci*. 1998;53:819–832.
28. Do DD, Do HD, Prasetyo I. Constant molar flow semi-batch adsorber as a tool to study adsorption kinetics of pure gases and vapors. *Chem Eng Sci*. 2000;55:1717–1727.
29. Sward BK, LeVan MD. Frequency response method for measuring mass transfer rates in adsorbents via pressure perturbation. *Adsorption*. 2003;9:37–54.
30. Glover TG, Wang Y, LeVan MD. Diffusion of condensible vapors in single adsorbent particles measured via concentration-swing frequency response. *Langmuir*. 2008;24:13406–13413.
31. Wang Y, LeVan MD. Nanopore diffusion rates for adsorption determined by pressure-swing and concentration-swing frequency response and comparison with Darken's equation. *Ind Eng Chem Res*. 2008;47:3121–3128.
32. Wang Y, LeVan MD. Mixture diffusion in nanoporous adsorbents: development of Fickian flux relationship and concentration-swing frequency response method. *Ind Eng Chem Res*. 2007;46:2141–2154.
33. Wang Y, LeVan MD. Investigation of mixture diffusion in nanoporous adsorbents via the pressure-swing frequency response method. 1. Theoretical treatment. *Ind Eng Chem Res*. 2005;44:3692–3701.
34. Wang Y, LeVan MD. Investigation of mixture diffusion in nanoporous adsorbents via the pressure-swing frequency response method. 2. Oxygen and nitrogen in a carbon molecular sieve. *Ind Eng Chem Res*. 2005;44:4745–4752.
35. Wang Y, Sward BK, LeVan MD. New frequency response method for measuring adsorption rates via pressure modulation: application to oxygen and nitrogen in a carbon molecular sieve. *Ind Eng Chem Res*. 2003;42:4213–4222.
36. Petkovska M, Markovic A. Fast estimation of quasi-steady states of cyclic nonlinear processes based on higher-order frequency response functions. Case study: cyclic operation of an adsorption column. *Ind Eng Chem Res*. 2006;45:266–291.
37. Petkovska M, Petkovska LT. Use of nonlinear frequency response for discriminating adsorption kinetics mechanisms resulting with bimodal characteristic functions. *Adsorption*. 2003;9:133–142.
38. Petkovska M, Do DD. Use of higher order FRFs for identification of nonlinear adsorption kinetics: single mechanisms under isothermal conditions. *Nonlinear Dyn*. 2000;21:353–376.
39. Petkovska M, Do DD. Nonlinear frequency response of adsorption systems: isothermal batch and continuous flow adsorber. *Chem Eng Sci*. 1998;53:3081–3097.
40. Bülow M, Schlodder H, Rees LVC, Richards RE. Molecular mobility of hydrocarbon ZSM5/silicalite systems studied by sorption uptake and frequency response methods. In: Murakami Y, Lijima A, Ward JW, editors. *New Development in Zeolite Science and Technology*. New York: Elsevier Science Publishing Company, Inc., 1986:579–586.
41. Shen DM, Rees LVC. Frequency response technique measurements of *p*-xylene diffusion in silicalite-1 and -2. *J Chem Soc Faraday Trans*. 1993;89:1063–1065.
42. Shen DM, Rees LVC. Study of fast diffusion in zeolites using a higher harmonic frequency response method. *J Chem Soc Faraday Trans*. 1994;90:3011–3015.
43. Shen DM, Rees LVC. Analysis of bimodal frequency-response behavious of *p*-xylene diffusion in silicalite-1. *J Chem Soc Faraday Trans*. 1995;91:2027–2033.
44. Song LJ, Rees LVC. Adsorption and transport of n-hexane in silicalite-1 by the frequency response technique. *J Chem Soc Faraday Trans*. 1997;93:649–657.
45. Bülow M, Shen DM. Sorption kinetics of atmospheric gases on Li,RE(rare earth)-LSX zeolite beads as sorbents for oxygen PVSA processes. *Micro Meso Mater*. 2007;105:163–169.
46. LeVan MD, Carta G. Adsorption and ion exchange. In: Green DW, Perry RH, editors. *Perry's Chemical Engineers' Handbook, 8th ed*. New York: McGraw-Hill, 2008:16–1–16–69.
47. Farooq S, Hassan MM, Ruthven DM. Heat effects in pressure swing adsorption system. *Chem Eng Sci*. 1988;43:1017–1031.
48. Mahle JJ, Friday DK, LeVan MD. Pressure swing adsorption for air purification. 1. Temperature cycling and role of weakly adsorbed carrier gas. *Ind Eng Chem Res*. 1996;35:2342–2354.
49. Walton KS, LeVan MD. Consistency of energy and material balances for bidisperse particles in fixed-bed adsorption and related applications. *Ind Eng Chem Res*. 2003;42:6938–6948.
50. Bourdin V, Gray PG, Grenier P, Terrier MF. An apparatus for adsorption dynamics studies using infrared measurement of the adsorbent temperature. *Rev Sci Instrum*. 1998;69:2130–2136.
51. Do DD. *Adsorption Analysis: Equilibria and Kinetics*. London: Imperial College Press, 1998.
52. Karger J, Ruthven DM. *Diffusion in Zeolites and Other Microporous Solids*. New York: Wiley, 1992.
53. Qinglin H, Sundaram SM, Farooq S. Revisiting transport of gases in the micropores of carbon molecular sieves. *Langmuir*. 2003;19:393–405.
54. Onyestyák G, Shen DM, Rees LVC. Frequency-response studies of CO_2 diffusion in commercial 5A powders and pellets. *Micro Mater*. 1996;5:279–288.

Appendix: Degenerate Forms of the General Model

The general model with three resistances described in Eqs. 61 and 62 can be reduced to the one or two resistance models in limiting cases of the parameters β_{bm} and β_{mM}, which are defined as relative ratios of the resistances. The general model is written

$$
\begin{aligned}
G_{\mathrm{n}}(s) &= \frac{\hat{\bar{n}}}{\bar{P}} = \frac{3 l_1 l_2'}{RT} \\
l_1 &= \frac{\sqrt{\eta_{\mathrm{m}}}\coth(\sqrt{\eta_{\mathrm{m}}}) - 1}{\eta_{\mathrm{m}}} \\
l_2' &= \frac{3\beta_{\mathrm{bm}} K}{s/\eta}\,\frac{\sqrt{s/\eta}\,\coth(\sqrt{s/\eta}) - 1}{\sqrt{s/\eta}\,\coth(\sqrt{s/\eta}) + \beta_{\mathrm{bm}} - 1} + \frac{\varepsilon_{\mathrm{p}}}{\rho_{\mathrm{p}}} \\
\eta_{\mathrm{m}} &= 3\beta_{\mathrm{mM}}\left[\sqrt{s/\eta}\,\coth(\sqrt{s/\eta}) - 1)\right] + \frac{\varepsilon_{\mathrm{p}}\beta_{\mathrm{mM}}}{\rho_{\mathrm{p}} K}\,\frac{s}{\eta}
\end{aligned}
\tag{A1}
$$

Micropore-macropore diffusion

The criteria for validity of this model is $\beta_{bm} \to \infty$. This gives

$$l_2' = \frac{3\beta_{bm}K}{s/\eta}\frac{\sqrt{s/\eta}\,\coth(\sqrt{s/\eta}) - 1}{\sqrt{s/\eta}\,\coth(\sqrt{s/\eta}) + \beta_{bm} - 1} + \frac{\varepsilon_p}{\rho_p}$$
$$= \frac{3K}{s/\eta}\frac{\sqrt{s/\eta}\,\coth(\sqrt{s/\eta}) - 1}{1 + (\sqrt{s/\eta}\,\coth(\sqrt{s/\eta}) - 1)/\beta_{bm}} + \frac{\varepsilon_p}{\rho_p}$$
$$\overset{\beta_{bm}\to\infty}{\to} \frac{3K}{s/\eta}\left[\sqrt{s/\eta}\,\coth(\sqrt{s/\eta}) - 1\right] + \frac{\varepsilon_p}{\rho_p} = l_2 \quad \text{(A2)}$$

from which follows Eqs. 58–60.

Macropore diffusion

The criteria for validity of this model are $\beta_{bm} \to \infty$ and $\beta_{mM} \to \infty$. The Taylor series expansion for coth z is

$$\coth z = \frac{1}{z} + \frac{z}{3} + O(z^3) \quad \text{(A3)}$$

With $\beta_{mM} \to \infty$ and the definition of β_{mM}, we obtain $\eta = D_s/r_s^2 \to \infty$ and $s/\eta \to 0$. Furthermore, η_m can be simplified with Eq. A3 to give

$$\eta_m = 3\frac{\rho K}{\varepsilon_p}\frac{D_s/r_s^2}{D_p/R_p^2}\left[\sqrt{s/\eta}\,\coth(\sqrt{s/\eta}) - 1)\right] + \frac{s}{D_p/R_p^2}$$
$$\overset{\beta_{mM}\to\infty}{\to} 3\frac{\rho K}{\varepsilon_p}\frac{D_s/r_s^2}{D_p/R_p^2}\left[(1/\sqrt{s/\eta} + \sqrt{s/\eta}/3)\sqrt{s/\eta} - 1\right]$$
$$+ \frac{s}{D_p/R_p^2} = \frac{s}{D_p/R_p^2}\left[\frac{\rho_p K}{\varepsilon_p} + 1\right] \quad \text{(A4)}$$

l_2, defined in Eq. 59, can be further reduced to

$$l_2 \overset{\beta_{mM}\to\infty}{\to} \frac{3K}{s/\eta}\left[\sqrt{s/\eta}\left(\frac{1}{\sqrt{s/\eta}} + \frac{\sqrt{s/\eta}}{3}\right) - 1\right] + \frac{\varepsilon_p}{\rho_p} = K + \frac{\varepsilon_p}{\rho_p} \quad \text{(A5)}$$

Substituting Eq. A5 into Eq. A1 gives the micropore-macropore G_n described by Eq. 46.

Micropore diffusion

The criteria for validity of this model are $\beta_{bm} \to \infty$ and $\beta_{mM} \to 0$. With the limitation of $\beta_{bm} \to \infty$, we derive the micropore-macropore model shown in Eq. A2. Substituting $\beta_{mM} \to 0$ into η_m, we have $\eta_m \to 0$. Thus, l_1 defined in Eq. 58 can be further reduced to

$$l_1 \overset{\beta_{mM}\to 0}{\to} \frac{\sqrt{\eta_m}(1/\sqrt{\eta_m} + \sqrt{\eta_m}/3)) - 1}{\eta_m} = 1/3 \quad \text{(A6)}$$

Combining with Eq. A2, we obtain the micropore diffusion model shown in Eq. 37.

Micropore-barrier diffusion

The criteria for validity of this model is $\beta_{mM} \to 0$. We substitute Eq. A6 into the general model to give the micropore-barrier resistance model described by Eq. 40.

LDF

The criteria for validity of this model are $\beta_{mM} \to 0$ and $\beta_{bm} \to 0$. With $\beta_{bm} \to 0$ and the definition of β_{bm}, we obtain $\eta = D_s/r_s^2 \to \infty$ and $s/\eta \to 0$. Substituting $\beta_{bm} = k_b r_s/D_s$ into Eq. 40 and simplifying gives

$$G_n(s) \overset{s/\eta\to 0}{\to} \frac{3Kk_b/r_s}{RT\,s}$$
$$\times \frac{1}{1 + (k_b r_s/D_s)/[\sqrt{s/\eta}(1/\sqrt{s/\eta} + \sqrt{s/\eta}/3) - 1]} + \frac{\varepsilon_p}{\rho_p RT}$$
$$= \frac{3Kk_b/r_s}{RT\,s}\frac{1}{1 + (3k_b/r_s)/s} \quad \text{(A7)}$$

For the barrier resistance existing at the entrance of the micropore, we have

$$\frac{d\tilde{n}}{dt} = \frac{3}{r_s^3}\int_0^{r_s}\left[\frac{D_s}{r^2}\frac{\partial}{\partial r}\left(r^2\frac{\partial n}{\partial r}\right)\right]r^2 dr$$
$$= \frac{3}{r_s}D_s\frac{\partial n}{\partial r}\Big|_{r_s}$$
$$= \frac{3}{r_s}k_b\Delta n \quad \text{(A8)}$$

With the barrier resistance described by the LDF model, the relationship between the barrier resistance k_B and the LDF coefficient k is $k = 3k_b/r_s$. Substituting this relationship into Eq. A7 gives the LDF model shown in Eq. 31.

Manuscript received July 30, 2010, and revision received Aug. 19, 2010.